The Astrophysical Journal, 927:71 (8pp), 2022 March 1 https://doi.org/10.3847/1538-4357/ac4d93
© 2022. The Author(s). Published by the American Astronomical Society.
OPEN ACCESS

A Model-independent Radio Telescope Dark Matter Search

Aya Keller[1], Sean O'Brien[1], Adyant Kamdar[1], Nicholas M. Rapidis[1,2], Alexander F. Leder[1], and Karl van Bibber[1]
[1] Department of Nuclear Engineering, University of California, Berkeley, CA 94709, USA; ayakeller@berkeley.edu
[2] Department of Physics, Stanford University, Stanford, CA 94305, USA
Received 2021 November 30; revised 2022 January 8; accepted 2022 January 18; published 2022 March 7

Abstract

A novel search technique for ultralight dark matter has been developed and carried out over a narrow range in the *L* band, utilizing the recent Breakthrough Listen public data release of three years of observation with the Green Bank Telescope. The search concept depends only on the assumption of decay or annihilation of virialized dark matter to a quasimonochromatic radio line, and additionally that the frequency and intensity of the line be consistent with most general properties expected of the phase space of our Milky Way halo. Specifically, the search selects for a line that exhibits a Doppler shift with position according to the solar motion through a static Galactic halo and similarly varies in intensity with the position with respect to the Galactic center. Over the frequency range 1.73–1.83 GHz, radiative annihilation of dark matter is excluded above $\langle\sigma v\rangle = 1.2 \times 10^{-47}\ \mathrm{cm^3\ s^{-1}}$ and for decay above $\lambda = 4.1 \times 10^{-35}\ \mathrm{s^{-1}}$. The analysis of the full Breakthrough Listen GBT data set by this method (25,000 spectra, 1.1-11.6 GHz) is currently underway.

Unified Astronomy Thesaurus concepts: Dark matter (353); Doppler shift (401); Radio astronomy (1338); Radio spectroscopy (1359); Technosignatures (2128)

1. Introduction

While the existence of dark matter has been firmly established, only limited progress has been made regarding its identification. One leading dark matter candidate is the weakly interacting massive particle (WIMP), the term broadly encompassing a range of beyond-standard model particles much heavier than the proton and with interaction cross sections at or below the weak scale. The most sensitive experiments today consist of ton-scale vessels of liquid xenon designed to detect both prompt scintillation and ionization from the rare scattering of these particles. Searches for WIMP dark matter have already excluded much of its parameter space (Akerib et al. 2014; Cui et al. 2017; Aprile et al. 2019). Another leading candidate is the axion, an ultralight particle with extraordinarily weak interactions to radiation and matter, arising from the most minimal solution to the strong-CP problem, i.e., the absence of a neutron electric dipole moment. The most sensitive experiments to the axion are based on their resonant conversion to quasimonochromatic photons in a microwave cavity permeated by a magnetic field, the expected signal strength being of order of yoctowatts. Axion searches, while finally possessing meaningful sensitivity within one decade of mass (Braine et al. 2020; Lee et al. 2020; Backes et al. 2021), now face theoretical mass bounds that have been recently relaxed by several orders of magnitude. Furthermore, a much broader theoretical framework for dark matter has emerged, spanning 10^{-22}–10^{-2} eV in mass, of which candidates such as the axion, represent but specific cases (Battaglieri et al. 2017). This presents a daunting experimental challenge, for which the broadened scope of dark matter theory calls for a similarly broadened approach in astrophysical observation in the hope of gleaning useful clues for the ultimate direct detection of dark matter. An optimal observational and analysis strategy should thus rely on as few general assumptions as possible, while possessing a high degree of selectivity and sensitivity to dark matter. This report proposes just such a search strategy and tests the concept over a narrow frequency range, analyzing spectra from a large data set and establishing exclusion limits for dark matter decay and annihilation in the *L* band. The analysis will then be implemented for thousands of spectra over a wide range of frequencies from the full Breakthrough Listen data set.

Original content from this work may be used under the terms of the Creative Commons Attribution 4.0 licence. Any further distribution of this work must maintain attribution to the author(s) and the title of the work, journal citation and DOI.

2. General Concepts

This search focuses on the possible radiative decay or annihilation of ultralight dark matter within our Milky Way Galactic halo, leading to a quasimonochromatic radio line ($\Delta\nu/\nu \approx 10^{-3}$). This search is further predicated on two generally accepted characteristics of dark matter in our Galactic halo. First, we assume that the dark matter constitutes a static halo through which our solar system is moving, with a characteristic velocity $v_S \approx 240\ \mathrm{km\ s^{-1}}$ tangential to the disk. Consequently, such a radio line would be distinguished from any other source, conventional or otherwise, by a systematic Doppler shift with respect to the Sun's direction of motion: (l, b) = (90°,0°) in Galactic coordinates. While our galaxy and its halo likely include nonvirialized streams of both baryonic and dark matter due to late-time assimilation of smaller galaxies, overall our halo should be well represented by a static virialized spherical distribution. Second, the signal should reflect the spatial distribution as represented by a standard halo model; more specifically the signal power should follow the line-integrated density of the halo ρ for dark-matter decay, or ρ^2 for annihilation or any other two-body process producing a photon. This implies that in an all-sky data set, a radio line representing a real dark matter signal should be maximized toward the Galactic center, (0°, 0°), minimized looking outward, and roughly symmetric around that axis.

Dark matter decay here includes all processes $\chi \rightarrow \phi + \gamma$, including in principle two-photon decays from pseudoscalars, such as the axion or an axion-like particle $\chi \rightarrow \gamma + \gamma$. For simplicity in calculating and presenting limits on the decay rate, λ, we will assume the photon energy $h\nu = \frac{m_\chi c^2}{2}$. What for convenience we refer to as annihilation similarly subsumes all

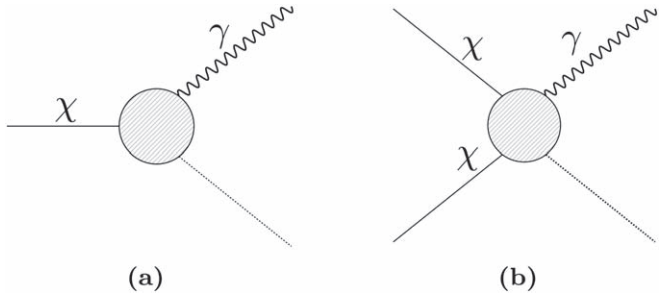

Figure 1. (a) Decay of a dark matter particle into a photon and another particle or photon. (b) Annihilation or Compton-like process leading to a two-body final state, one of which is a photon.

two-body initial states, including annihilation proper $\chi + \chi \rightarrow \phi + \gamma$ as well as Compton-like processes $\chi + \xi \rightarrow \phi + \gamma$, where ξ and ϕ represent any standard model or beyond-standard model particles; see Figure 1.

3. The Breakthrough Listen Data Set

This analysis utilizes the Breakthrough Listen (BL) public data release from the 100 m Robert C. Byrd Green Bank radio telescope (GBT), which was taken between 2016 January and 2019 March (Lebofsky et al. 2019; Price et al. 2020). The BL program to date has focused on approximately 1700 nearby Hipparcos catalog stars, as well as some targets from other catalogs that were not used for this analysis (Perryman et al. 1997; Isaacson et al. 2017) and 100 nearby galaxies. Observations with the GBT have been taken with receivers covering the *L*, *S*, *C*, and *X* bands (1.1–11.6 GHz), with the analysis described in this report being limited to the high end of the *L* band, 1.71–1.84 GHz. The *L*- to *X*-band range lends itself favorably to a search for monochromatic photons from dark matter, as the region is largely devoid of molecular lines, and radio frequency interference (RFI) lines are largely confined to the lower frequencies, whose identification can be confirmed by the GBT RFI scan archive (Murphy 2019).

The BL observing cadence for each star comprises six 5 minute spectra with the pattern ABACAD, where A designates an on-target spectrum, with B, C, and D designating different off-target spectra, each a few degrees away from the target and from one another. All spectra A, B, C, D were included in the analysis, whether catalog stars or dark sky, after carefully examining for any evidence for differences between pairs of spectra, whether on- and off-star, or between pairs of distinct stars. Such contributions, which might bias the analysis, could be either from conventional astrophysics (or extraterrestrial communication, technosignatures etc., as the Breakthrough Listen survey was conducted in support of the SETI program). We conclude that the catalog stars in this survey were radio-quiet for the purposes of this study, and thus all spectra were included. The BL on-off observing strategy was designed for optimal subtraction of common background. Under the assumption that dark matter is smoothly distributed in the halo and not preferentially localized around any particular star, all spectra collected are useful to our analysis, independent of specific coordinates. The spectrograms used in this analysis have an intrinsic channel resolution of approximately 2.8610 kHz and are imprinted with the polyphase filter-bank structure, a symmetric bandpass function repeated every 1024 channels in the spectrogram data, or approximately 2.93 MHz. The spectra are additionally characterized by a quasi-periodic $\approx$15 MHz undulation, approximately 10% in magnitude. As will be described later, to usefully combine and manipulate thousands of spectra in our analysis requires that both the polyphase filter and undulatory structure be removed, as well as drifts in both shape and magnitude, evident even between successive 5 minute observations. Clearly, the uniqueness of the BL data set for a general dark matter search is the total integration time it represents: three months of total broadband observation covering the entire sky accessible to the GBT.

4. Detailed Description of the Analysis

This is not the first search for dark matter based on its decay to a quasimonochromatic radio line (Blout et al. 2001; Foster et al. 2020), and future radio searches are under study. Our approach differs insofar as it is not restricted to specific particle candidates, specific mechanisms, or to specific astrophysical sites, but is model-independent and utilizes the entire BL data set comprehensively covering the Milky Way.

Before descending into details of the analysis, a step-by-step overview may be helpful to understand how limits on dark matter lifetimes and annihilation cross sections are derived. (i) First, the individual spectrograms are unit-normalized by a procedure that preserves the structure of the expected signal width and rebinned. (ii) The Doppler asymmetry spectrum is formed based on sorting the overall sample of spectra into Forward and Backward populations, relative to the Sun's vector velocity in the MW. The intensity asymmetry spectrum is similarly formed, relative to the vector to the Galactic center. (iii) For the halo model assumed with its specific parameters, the line integrals and Doppler shifts associated with the Galactic coordinates of each spectrum included in the samples above are calculated. Templates for the Doppler and intensity asymmetries are calculated specific to the spectra included in the analysis. (iv) The Doppler and intensity correlation spectra are formed by taking the dot product between their asymmetry spectra and templates at each frequency. (v) Finally the Doppler and intensity correlation spectra themselves are cross correlated, and physics limits are established based on a p-value analysis.

The cases of dark matter decay and annihilation will be treated separately, as their observed line widths will differ. Assuming a static halo of uniform virial velocity, the Doppler broadening of the source along the line of sight for the two cases is given by

$$\frac{\sigma_D}{\nu} = \frac{\sigma_{\rm vir}}{\sqrt{3}\,c} \quad \text{and} \quad \frac{\sigma_A}{\nu} = \frac{\sigma_{\rm vir}}{\sqrt{6}\,c}, \tag{1}$$

where σ_D and σ_A denote the standard deviation in frequency associated with decay and annihilation, respectively, and $\sigma_{\rm vir}$ the virial velocity of the halo. Being the sum of Gaussian variates, the distribution of the two-body center of mass motion is narrowed by $\sqrt{2}$ relative to that of a single particle, and thus the line width for dark matter annihilation is correspondingly narrowed relative to decay.

For each frequency band, this analysis requires the combining of thousands of spectra taken over a year or more, at differing times of day, sky position, atmospheric conditions, hardware and software configurations, etc. Both the shape and magnitude of the spectra varied by several percent and often much more, even between sequential 5 minute observations taken only a few degrees apart. To search for a very small

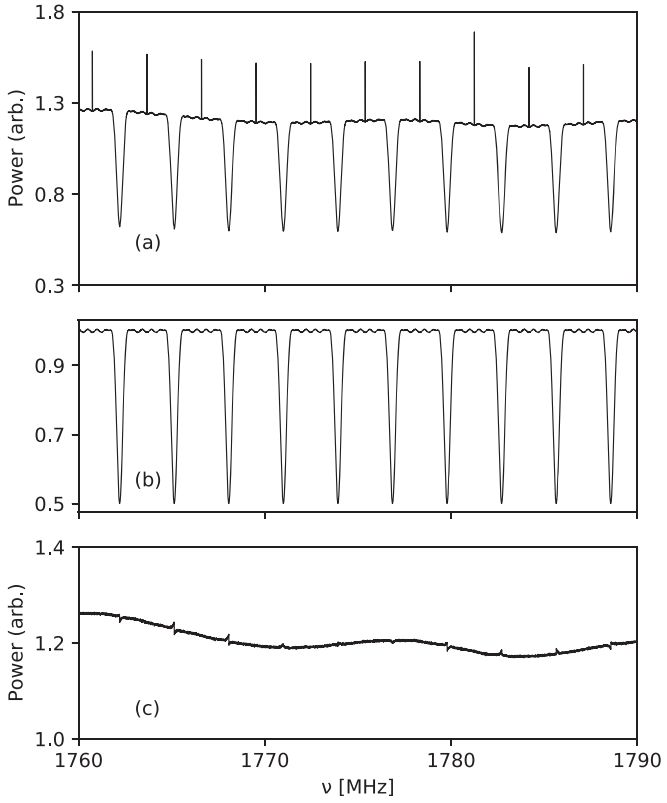

Figure 2. (a) Part of a typical spectrogram in the *L* band. (b) The polyphase filter function (PPF). (c) The spectrum after removing the PPF. Note the discontinuities associated with the adjoining 1024-channel polyphase filterbank bandpass functions; ±48 channels are excised at those frequencies before fitting and normalizing the spectra.

signal aggregated over such a large data set first required unit-normalization of the data. The first step in the analysis consists of dividing the spectrograms by the polyphase filter function (PPF) and excising 48 points at the beginning and end of each of the repeated 1024-channel bandpass response. The deep periodic minima observed in the spectrograms reflect where the neighboring bandpass functions roll off; data points around these minima are characteristically unstable and need to be removed before fitting (Figure 2).

The spectra are then co-averaged by 64 channels; this results in both improved sensitivity in the final analysis but more importantly a major reduction in computational time in the fitting procedure. Next, the spectra are unit normalized by forming a ratio of polynomial fit to the PPF-corrected spectrum within a window around each data point in the spectrum:

$$R(\nu_i) = \frac{P(\nu_i;\, m,\, n;\, 0,\, 0)}{P(\nu_i;\, m,\, n;\, a,\, b)}. \tag{2}$$

For the polynomial $P(\nu_i; m, n; a, b)$ fit to the data within a window around ν_i, m is the number of data points within the window, and n is the order of the polynomial. The values $(m, n) = (53, 5)$ were selected on the basis of maximizing the signal to noise of the spectral asymmetry for synthetic signals injected into the spectrum, as described below. This was done with a sparse grid search, and more advanced optimization of these parameters will be done for the full analysis. Parameters (a,b) are the standard Gaussian function parameters that determine the de-weighting function applied to the data points

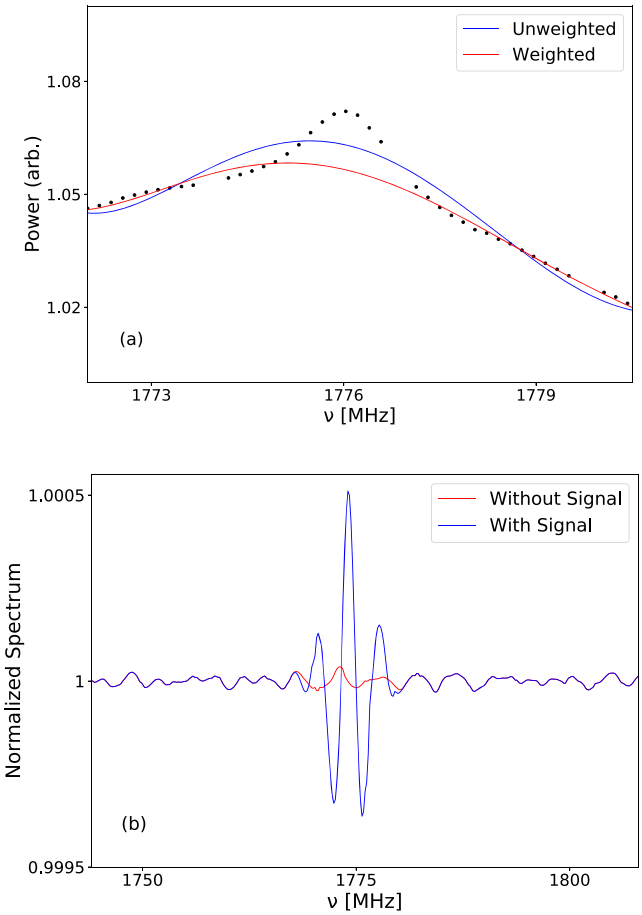

Figure 3. (a) A synthetic signal from dark matter annihilation with velocity-weighted cross section $\langle\sigma v\rangle = 4 \times 10^{-43}\,\mathrm{cm^3\,s^{-1}}$ injected into one raw spectrogram, with the corresponding weighted and unweighted polynomial fits. (b) The resulting normalized spectra for the cases with and without the injected signal.

within the rolling window around ν_i:

$$W(\nu,\, \nu_i) = 1 - a \cdot \exp\left[\frac{-(\nu - \nu_i)^2}{2b^2\sigma^2_{A,D}(\nu_i)}\right]. \tag{3}$$

For the unweighted polynomial in the numerator, the fit more closely tracks any signal atop the local background, whereas the de-weighted polynomial is desensitized to any putative signal around ν_i and thus more closely interpolates the real background in the absence of such a signal. Intuitively, one might expect that $b \approx 1$ would be an appropriate choice to accentuate a signal with an expected width of $\sigma_{A,D}$; ultimately $(a,\, b) = (0.1,\, 1)$ were found to give satisfactory results and were used in this analysis. Figure 3 shows both the unweighted and weighted polynomials in the vicinity of an injected annihilation signal for a velocity-weighted cross section $\langle\sigma v\rangle = 4 \times 10^{-43}\,\mathrm{cm^3\,s^{-1}}$ and the resulting normalized spectrum both with and without the injected signal.

Two points should be noted about the normalization method adopted for this analysis. First, as with many such schemes, the fitting procedure transforms a simple signal shape (here a Gaussian) superposed on a smooth background into a more complex form. This does not represent a fundamental problem, as the overall analysis can be adequately modeled. Second, as the normalization scheme is optimized to accentuate the signal, it also

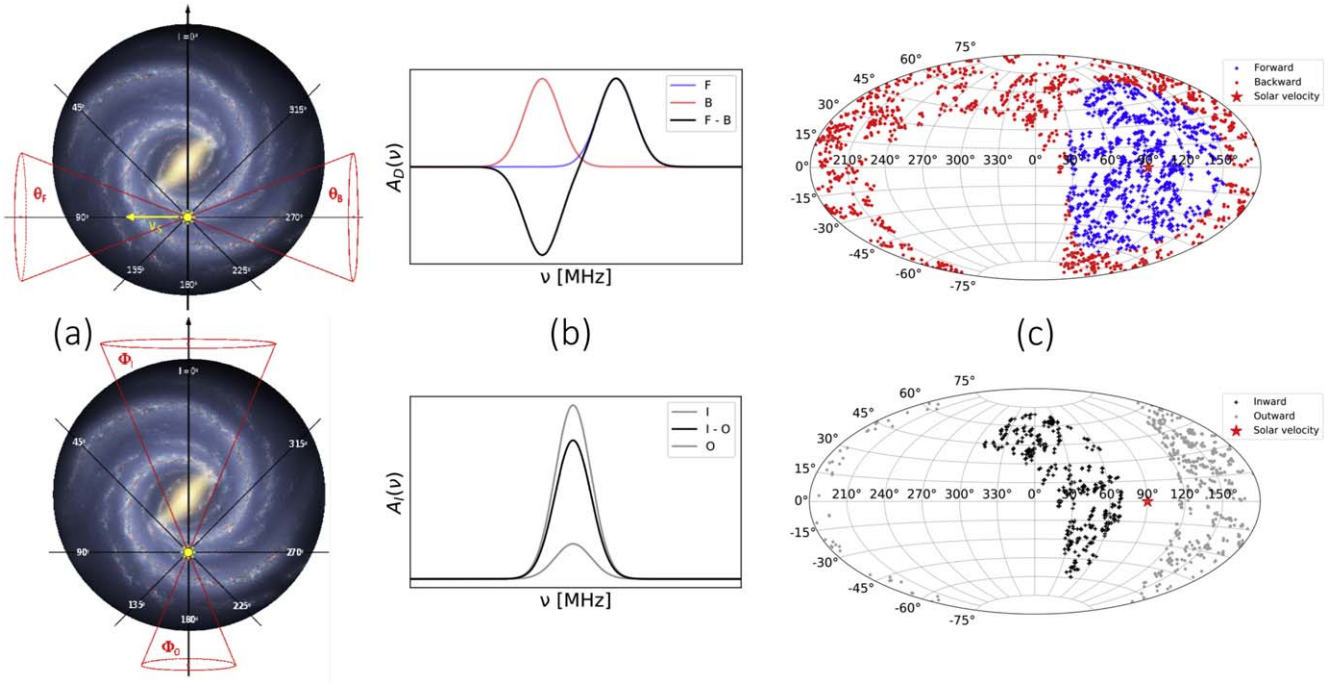

Figure 4. (a) Concept of asymmetry-based searches for dark matter within a large data set broadly sampling the observable sky. The angles defining the Forward and Backward samples, $\theta_{F,B}$ are chosen to maximize the signal-to-noise ratio. (b) The idealized dark matter signature in the Doppler asymmetry spectrum $A_D(\nu)$ would be a bipolar signal in frequency, prescribed by the (V_S, $\sigma_{\rm vir}$) and the ensemble of specific targets selected. The idealized dark matter signature in the intensity asymmetry spectrum $A_I(\nu)$ would be a unipolar signal centered at the frequency of the decay or annihilation photon in the dark matter's rest frame. (c) Mercator plots exhibiting the actual targets included in the analysis, the regions being demarked by θ_F = closeup $\theta_B = 65°$ and $\theta_I = 70°$, $\theta_O = 115°$.

accentuates the residual structure associated with imperfect removal of the polyphase filterbank bandpass response, as in this frequency range, they are of the same order in width, i.e., a few MHz. This is a more significant problem, but which the asymmetry analysis significantly cancels out.

The concept of the Doppler and intensity asymmetries is schematically represented in Figure 4. In the case of the Doppler asymmetry, under the assumption of a static halo, a dark matter signal is Doppler shifted according to its polar angle θ from the direction of the Sun's motion through the galaxy,

$$\nu' = \nu\left(1 + \frac{V_S}{c} \cdot \cos\theta\right), \tag{4}$$

where estimates for the solar velocity $V_S \approx 240$ km s^{-1} (Monari et al. 2018) are comparable to the local virial velocity of the galaxy, $\sigma_{\rm vir} \approx 270$ km s^{-1} (Pillepich et al. 2014). Owing to the observational and modeling uncertainties intrinsic to these numbers, we explore the sensitivity of our analysis to excursions of V_S and $\sigma_{\rm vir}$ within the range 225–275 km s^{-1} and find it to be very stable.

For each case, the asymmetry spectrum is formed:

$$A_D(\nu) = \frac{F - B}{F + B} \quad A_I(\nu) = \frac{I - O}{I + O}, \tag{5}$$

with F (B) designating the average of all spectra within the Forward (Backward) acceptances defined by their polar angles $\theta_{F/B}$.

$$F(\nu, \theta_F) = \frac{1}{n_f}\sum_i f_i(\nu) \quad B(\nu, \theta_B) = \frac{1}{n_b}\sum_i b_i(\nu), \tag{6}$$

for some fixed θ_F and θ_B and similarly for I (O), the Inward (Outward) populations within their respective polar angle cuts $\Phi_{I/O}$. Forming asymmetry spectra has the virtue of canceling out to a high degree common-mode residual structure apparent in all normalized spectra at the $\approx 10^{-4}$ level, thus enabling a more sensitive search.

We wish to note that this is not the first proposed use of a Doppler shift as a discriminant of dark matter; see Speckhard et al. (2016) for its suggested application in regard to the 3.5 keV line reported by several X-ray observatories.

4.1. Doppler Asymmetry Analysis

The flux density in general for the two cases of annihilation and decay processes is given by:

$$\frac{P_A}{\Delta A \Delta \nu} = \frac{1}{8\sqrt{2\pi}} \frac{\langle \sigma v \rangle (\Delta\theta)^2 c^2}{M_\chi \eta^A \nu_0} e^{\left[-\left(\frac{\nu-\nu_0}{\sqrt{2}\eta^A \nu_0}\right)^2\right]} \int_0^\infty \rho(\mathbf{r})^2 \, d\mathbf{r}, \tag{7}$$

$$\frac{P_D}{\Delta A \Delta \nu} = \frac{1}{16\sqrt{2\pi}} \frac{\lambda (\Delta\theta)^2 c^2}{\eta^D \nu_0} e^{\left[-\left(\frac{\nu-\nu_0}{\sqrt{2}\eta^D \nu_0}\right)^2\right]} \int_0^\infty \rho(\mathbf{r}) \, d\mathbf{r}, \tag{8}$$

which depends on the particle physics through the velocity-weighted cross section $\langle \sigma v \rangle$ for annihilation, or the decay constant λ in the case of decay. Here η is the line width with $\sigma_{\rm vir}$ the halo viral velocity, $\rho(\boldsymbol{r})$ the halo density along the line of sight, and $\Delta\theta$ the frequency-dependent FWHM beamwidth of the telescope.

$$\eta^A = \frac{\sigma_{\rm vir}}{\sqrt{6}\,c}, \quad \eta^D = \frac{\sigma_{\rm vir}}{\sqrt{3}\,c}. \tag{9}$$

For simplicity, these formulae are written for the special case of a two-photon final state, i.e., $\chi\chi \to \gamma\gamma$ and $\chi \to \gamma\gamma$, for which the resulting limits will be seen to be much weaker than allowed by stellar evolution but are readily convertible to limits for final states with a massive particle $\phi\gamma$. For the development and demonstration of this analysis, we selected a limited range of the BL *L*-band data, 1710–1850 MHz, as it was relatively free of RFI or molecular lines; two narrow RFI peaks were identified and excised from the spectrograms. This was done by filtering for peaks that appeared consistently in most spectrograms and were no wider than three channels, as the signals we are searching for are hundreds of channels wide in the spectrograms before co-averaging. After the normalization of the data, a cut was made on the standard deviation to minimize statistical noise and residual structure, yielding approximately 4400 spectra.

The resulting limits are derived by a standard matched-filtering technique. A template of the asymmetry for a dark matter signal is created at each frequency ν in the spectrum, $\boldsymbol{T}(\nu)$, specific to the particle physics input $\langle\sigma v\rangle$ or λ, target samples $\theta_{F/B}$, Galactic parameters (V_S, $\sigma_{\rm vir}$), and halo model. This involves calculating the contribution of the expected signal for each target (Equations (7), (8)), transforming the input Gaussian line into the actual shape as it appears in the normalized spectrum, applying the coordinate-dependent Doppler shift (Equation (4)), and finally summing and forming the asymmetry (Equations (6), (5)). At each frequency ν the template is integrated over the asymmetry spectrum:

$$R_D(\nu) = \boldsymbol{T}\cdot\boldsymbol{A_D}(\boldsymbol{\nu}) \equiv \sum_{\nu'} T(\nu-\nu')A_D(\nu-\nu'), \tag{10}$$

resulting in the Doppler correlation spectrum $R_D(\nu)$.

Limits are derived by injecting synthetic signals at the raw spectrogram level, carrying through the analysis as described, and establishing the confidence level against the statistical distribution of $R(\nu)$ in the absence of a signal. (As limits are derived by comparison of the Doppler correlation spectrum with and without signal injection, the results depend only on the shape of the template; the absolute magnitude is immaterial.) The signal-to-noise ratio (S/N) is maximized by utilizing all of the data after the data quality cut, and equalizing the Forward and Backward populations, corresponding to the polar angle $\theta_F = \theta_B = 65°$ (Figure 5).

For each frequency bin, the limit on the velocity-weighted cross section (99.7% c.l.) is that corresponding to $3\sigma_{\rm corr}$ of the Doppler correlation spectrum without injection of the signal; at 1775 MHz, as exhibited in Figure 5, $\langle\sigma v\rangle = 7.8 \times 10^{-45}\,{\rm cm^3\,s^{-1}}$. Three comments are in order concerning determination of the limits. First, as the BL data set was lacking in any useful calibration targets, the system equivalent flux density (SEFD) was calculated from the published GBT *L*-band system noise temperature of $T_{\rm SYS} = 20$ K and aperture efficiency 70%. To check our absolute calibration, a comparison was made of the inferred H I column density measured in our data with data from the Bonn Library (Ben Bekhti et al. 2016). The inferred value is within 1.5% of the older Leiden/Argentine/Bonn (LAB) survey and 15% higher than the newer Effelsburg/Bonn H I survey (EBHIS), thus giving us confidence in our procedure. Second, while the Doppler correlation function over this narrow frequency range is reasonably described as Gaussian-distributed (Figure 5 inset), the first full-scale analysis (*S* band, 1.7–2.8 GHz) will constitute a more critical test. Third, the limit above was derived with a search template of the same Galactic halo parameters as the injected signal, $(V_S, \sigma_{\rm vir}) = (225, 250)$ [km s^{-1}]. As we have no precise à priori knowledge of the halo parameters, the actual full analysis will include a search over a sparse grid within current bounds of solar and virial velocities, e.g., $(V_S, \sigma_{\rm vir}) = (200, 225, 250) \otimes (225, 250, 275)$ [km s^{-1}]. To estimate the sensitivity of the analysis to our ignorance of halo parameters, we have injected a signal with a significantly different choice of halo parameters within this grid, $(V_S, \sigma_{\rm vir}) = (250, 225)$ [km s^{-1}], but performed the search for a template of (225, 250); the limit for this case was in fact improved by ≈7% owing to the increase in the signal size corresponding to the velocities used for injection. Analyzing the data under the assumption of dark matter decay, where the width in frequency is increased by $\sqrt{2}$ relative to the two-body initial state (assuming equal-mass particles), the limit on the decay rate (99.7% c.l.) is $\lambda = 2.7 \times 10^{-32}\,{\rm s^{-1}}$ with $(V_S, \sigma_{\rm vir}) = (225, 250)$ [km s^{-1}] for both the injected signal and template.

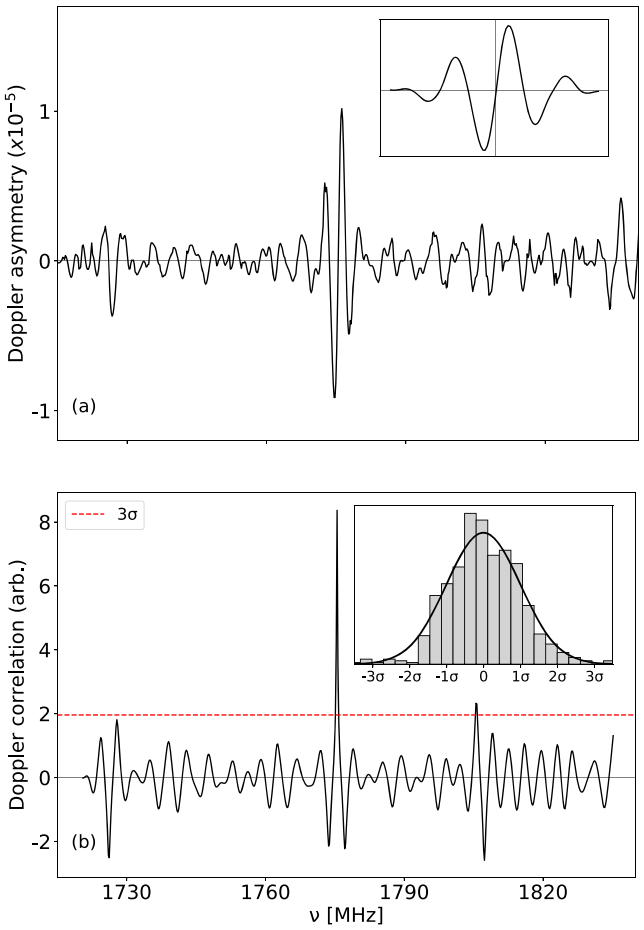

Figure 5. (a) Doppler asymmetry spectrum for the case $V_S = 225$ km s^{-1}, $\sigma_{\rm vir} = 250$ km s^{-1}, for $\nu = 1775$ MHz, and a velocity-weighted cross section $\langle\sigma v\rangle = 4.0 \times 10^{-44}$ cm^3 s^{-1} shown for scale. (Inset) Template formed for current parameters. (b) The Doppler correlation spectrum. (Inset) Doppler correlation spectral distribution in units of standard deviation $\sigma_{\rm corr}$ in the absence of a signal.

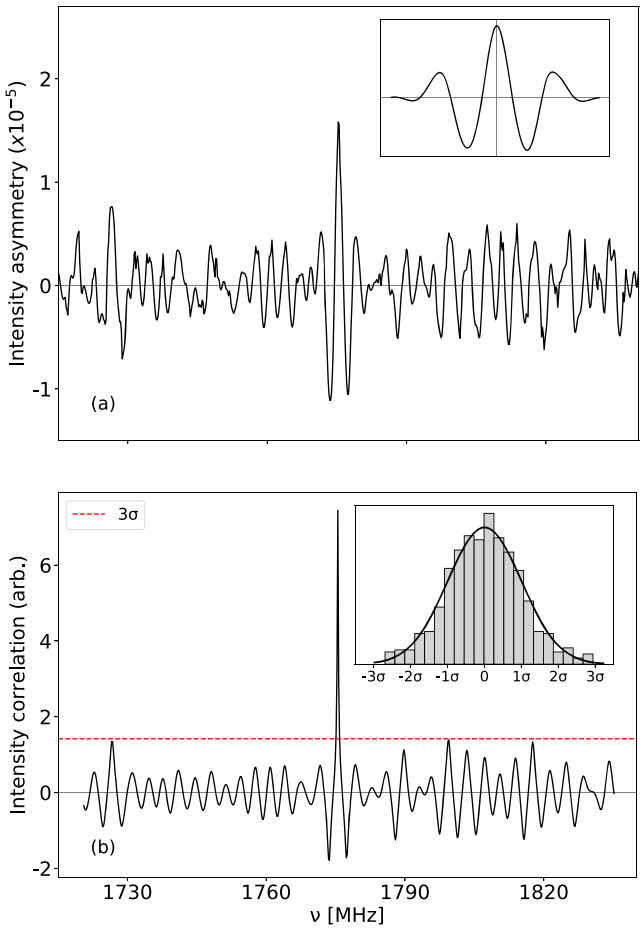

Figure 6. (a) Intensity asymmetry spectrum. (b) Intensity correlation spectrum and its spectral distribution, for the same case as in Figure 5.

4.2. Intensity Asymmetry Analysis

The analysis based on the expected signal asymmetry between looking inward (I), toward the Galactic center and outward (O), away from the Galactic center follows in an essentially identical manner. As mentioned previously, here the S/N is maximized by more tightly restricting the cone defining the inward population, and leaving a large gap in angle ($\theta_I = 70^\circ$ $\theta_O = 115^\circ$). For this first analysis, a Navarro–Frenk–White (NFW) halo was used (Navarro et al. 1997; Nesti & Salucci 2013):

$$\rho(r) = \rho_c \left(\frac{r}{r_c}\right)^{-1} \left(1 + \frac{r}{r_c}\right)^{-2}, \tag{11}$$

with $\rho_c = 1.4 \times 10^7\, M_\odot \mathrm{kpc}^{-3}$ and $r_c = 16.1$ kpc.

Stronger limits can be achieved by cross-correlating the Doppler and intensity analyses, ensuring that the two analyses are absolutely independent. In particular, it is most important to ensure that there are no remnant velocity correlations inadvertently built in to the I,O populations of the intensity analysis, owing to the incomplete GBT Galactic coverage (Figure 4). To ensure that the total I,O contributions (Equation (6)) were coincident in frequency, that is, free of residual Doppler shift, while maximizing the number of spectra selected (here 1581), the Hungarian matching algorithm is used (Kuhn 1955).

Figure 6 shows the corresponding intensity asymmetry $A_I(\nu)$ and intensity correlation $R_I(\nu)$; in comparison with the Doppler analysis for the case of injection and search at $(V_S, \sigma_{\rm vir}) = (225, 250)$ [km s^{-1}], the intensity analysis yields a comparable but slightly stronger limit for the annihilation case, $\langle\sigma v\rangle = 2.0 \times 10^{-45}\,\mathrm{cm}^3\,\mathrm{s}^{-1}$ similarly for the decay case, $\lambda = 1.6 \times 10^{-32}\,\mathrm{s}^{-1}$.

4.3. Combined Analysis

The results of the separate Doppler and intensity analyses can be combined to yield stronger limits on halo dark matter. As the analyses are independent and their individual template correlation spectra are Gaussian distributed, application of the p-test on the cross correlation of the two analyses is straightforward. Figure 7 shows that the annihilation limit is in fact significantly improved at 1775; this is the case across the entire spectrum, whether at specific frequencies the Doppler limit is stronger than the intensity limit or vice versa. (As the Doppler correlation spectrum was formed with the F,B populations divided at $\theta_{F,B} = 65^\circ$, the spectrum was back-projected to $\theta_{F,B} = 90^\circ$ to remove the small residual Doppler shift, thus ensuring that any signal would appear at its rest-frame frequency in both the Doppler and intensity correlation spectra.)

It may be inquired to what degree the physics exclusion limits depend on the exact choice of halo model. We have performed such a comparison between those derived from the NFW halo described above, and those from a Burkert halo, the parameters of which were determined by fitting to the same Milky Way Galactic observables by the same authors (Nesti & Salucci 2013). Whereas the NFW represents a cuspy halo, divergent at the Galactic center, the Burkert model represents a cored halo with a central density of $4.13 \times 10^7\, M_s\,\mathrm{kpc}^{-3}$, where M_s is the solar mass. While both yield essentially the same local density, the quantity of interest to direct detection experiments, $\rho^{\rm NFW}(r_s) = 0.471$ GeV cm^{-3} and $\rho^{\rm Bur}(r_s) = 0.487$ GeV cm^{-3}, their virial masses $M_{\rm vir}$ differ considerably, $1.53 \times 10^{12}\, M_s$ and $1.11 \times 10^{12}\, M_s$, respectively. As our radio survey method is sensitive to both the halo distribution and its total mass, it is not surprising then that the physics limits will vary with the choice of halo model and in fact the limit on the annihilation cross section for the Burkert model at 1775 MHz being weaker by 60%. Analogous uncertainties in direct detection limits arise from differing assumptions of local halo density, which varies among reports from 0.3 to 0.6 GeV cm^{-3}. Our specific choice of the NFW model here was arbitrary and solely for the purposes of demonstration.

5. Discussion

This study conducted over a limited frequency range in the L band establishes the feasibility of a selective and sensitive search for a broad, isotropic dark matter signal based on only very general properties of the halo.

Once given specific choices of V_S, $\sigma_{\rm vir}$, and the halo model, the frequency shift and magnitude of an expected signal are uniquely prescribed for each target, up to the unknown physics parameter $\langle\sigma v\rangle$ or λ. It may be asked then, whether a more powerful search procedure would be to do a global least squares fit summed over all spectra, to the single desired physics parameter $\langle\sigma v\rangle$ or λ. In principle, it should yield better limits, as it maximally utilizes the frequency–intensity

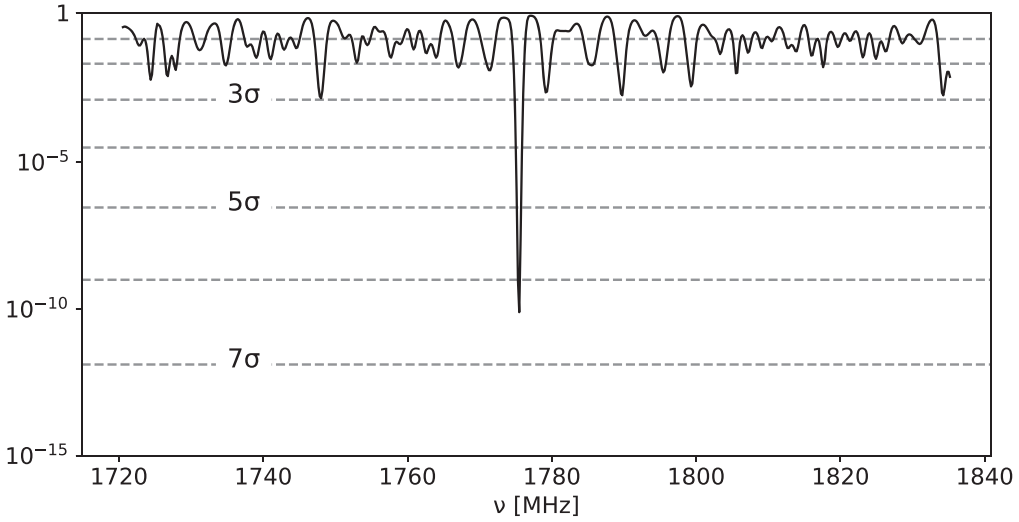

Figure 7. The p-statistic over the full data range of this study, for the annihilation case; (V_S, $\sigma_{\rm vir}$) = (225, 250) [km s^{-1}] for both the injected synthetic signal and search template, and $\langle\sigma v\rangle = 6 \times 10^{-45}$ cm^3 s^{-1}.

correlation for each target (l,b), rather than in aggregate. Such a procedure was attempted, but the results were worse than those presented above. The reason is that the normalized spectra all have a small common periodic residual structure, ultimately due to the imperfect removal of the polyphase filter-bank function, readily apparent in a 2D plot of the spectra (i.e., the spectra plotted as a surface in the cos(θ)-ν plane) as a "washboard" residual at the $\approx 10^{-(3-4)}$ level. For the same reason, attempts to identify a signal of interest in a 2D representation of the data (cos(θ) versus ν), manifesting as a line of slope corresponding to an appropriate Doppler shift were equally unpromising, even with feature extraction techniques, such as the Hough transform and its modern extensions. The asymmetry-based analyses based on differences and ratios, however, effectively cancel this structure out, resulting in improved limits.

The limits presented above were derived for a spontaneous decay or annihilation process, in the absence of any radiation field. Clearly this situation never pertains in an astrophysical or cosmological context where these processes take place in a radiation background of multiple components. Caputo et al. have calculated the stimulated emission of axions within the radiation background of our Galactic halo (Caputo et al. 2019), but the results are readily generalized to any process with a photon in the final state. Specifically, the enhancement for the rate or cross section is a simple multiplicative factor of $2f_\gamma$, or f_γ if there is only a single photon in the final state, where f_γ is the photon occupation number. For our halo,

$$f_\gamma = f_{\gamma,\rm CMB}(\nu) + f_{\gamma,\rm ext-bkg}(\nu) + f_{\gamma,\rm gal}(\nu; l, b), \qquad (12)$$

where the three components represent the cosmic microwave background ($T_{\rm CMB} = 2.725K$), the extragalactic radio background ($T_{\rm ext-bkg} \approx 0.78K$ in the middle of our frequency range), and the Galactic diffuse emission. The CMB and the extragalactic radio background are isotropic, whereas the Galactic diffuse emission is sharply peaked around the Galactic center, which being largely below the GBT horizon, can be neglected for this analysis. Over our frequency range, $2f_\gamma \approx 68$; the resulting limit for a two-photon decay (i.e., an axion-like particle) is 4×10^{-35} s^{-1} (Figure 8(b), dashed line),

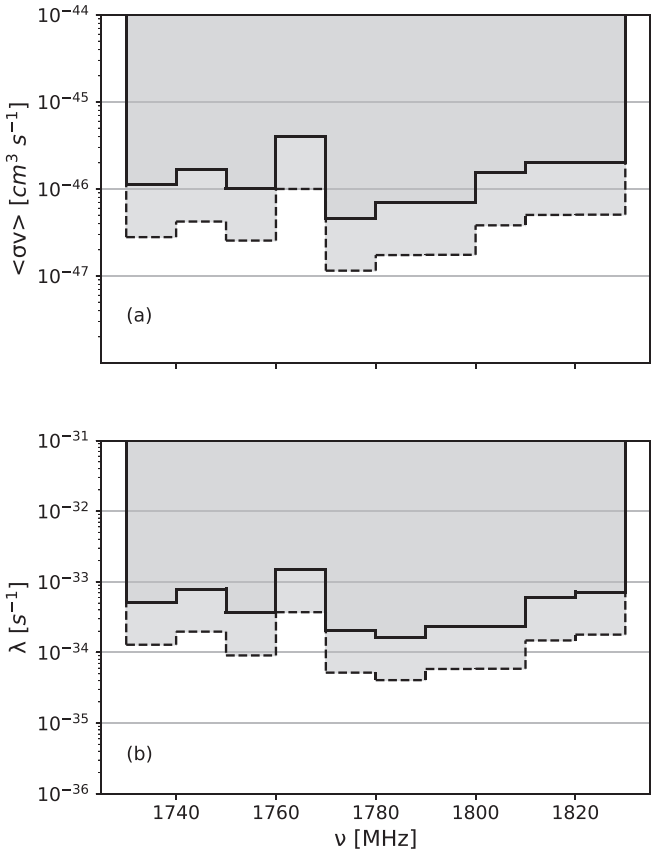

Figure 8. Limits from the combined asymmetry analysis for the cases of dark matter (a) annihilation and (b) decay within our Galactic halo with (V_S, $\sigma_{\rm vir}$) = (225, 250) [km s^{-1}] for both the injected synthetic signal and search template. Solid line: 1 photon final states. Dashed line: 2 photon final states. All limits here include the stimulated emission enhancement factor as described in the text (Caputo et al. 2019).

corresponding to an axion-photon decay constant of $g_{a\gamma\gamma}$=4.1×10^{-8} GeV^{-1}. While comparable to the best laboratory experiment based on photon regeneration (Ballou et al. 2015), it is weaker by 3 orders of magnitude than bounds from the CERN Axion Solar Telescope (CAST) axion helioscope

(Anastassopoulos et al. 2017) and horizontal branch star limits (Ayala et al. 2014). The single-photon limits are weaker by a factor of 4 (Figure 8(b), solid line), but are immune from stellar evolution limits based on the Primakoff effect. These include all processes $\chi \rightarrow \phi\gamma$, $\chi\xi \rightarrow \phi\gamma$, where $\phi \neq \gamma$; such decays for axions and axion-like particles have been studied by several authors (Kaneta et al. 2017).

It may be wondered what the ultimate sensitivity of this analysis could be. Absent a more accurate determination of the PFF to be divided out from the spectrograms, the PPF will remain the dominant limitation to our sensitivity, as the residual structure associated with imperfect knowledge of its form is of the same order width as the expected signal in this frequency range. As our normalization scheme is designed to protect structure of the expected width of the dark matter signal, O (MHz) in our frequency range, but eliminates broader structures and continuum contributions such as sky temperature. Unidentified RFI, which is constant in frequency and time, will cancel out of the Doppler asymmetry, but episodic RFI represents a potential limitation. Barring that, the exclusion region could ultimately be statistically limited.

For simplicity, the analysis above has been carried out assuming two-photon final states, and only for annihilation in the case of two-body initial states, which are of equal mass by construction. The results are readily generalized when deviating from these assumptions. In regard to the frequency dispersion of the search template, whereas for annihilation one expects a narrowing relative to the decay width of $\sigma_A = \sigma_D/\sqrt{2}$, for the asymmetric case $m_\xi \neq m_\chi$,

$$\frac{\sigma_D}{\nu} = \frac{\sigma_V}{\sqrt{3}\,c}\left[\left(\frac{m_\chi}{M}\right)^2 + \left(\frac{m_\xi}{M}\right)^2\right]^{\frac{1}{2}}, \tag{13}$$

with $M = m_\xi + m_\chi$; note the bracketed factor is $\frac{1}{\sqrt{2}}$ for $m_\chi = m_\xi$ but approaches 1 for $m_\xi << m_\chi$. Thus anticipating all possibilities, including e.g., a Compton-like process involving an ultralight dark matter particle and a standard-model particle, annihilation of two dark matter particles, etc., one needs to carry out the analysis for the range of frequency dispersions between these two limits.

Also, in the case of a decay of a dark matter particle of mass m_χ to a final state of a particle of mass m_ϕ and a photon, the photon energy is given by $E_\gamma = \frac{(m_\chi^2 - m_\phi^2)c^2}{2m_\chi}$. As in the absence of other information concerning ϕ, the initial mass is unknown, the constraint on the actual decay rate $\lambda_{\phi,\gamma}$ and initial mass m_χ are coupled, $\lambda_{\phi,\gamma} = \lambda_{\gamma,\gamma}\frac{m_\chi c^2}{2E_\gamma}$, where $\lambda_{\gamma,\gamma}$ is the rate inferred assuming two-photon decay as shown in Equation (8).

The future Square Kilometer Array (SKA) will have the benefit of the very large Bose–Einstein enhancement factor associated with the Galactic diffuse emission ($2f_\gamma \approx 10^{(3-4)}$ for the comparable L-band range as studied here), which could result in sensitivity exceeding the current horizontal branch star and CAST limits (Anastassopoulos et al. 2017). Whether the analysis techniques explored here, particularly the Doppler asymmetry, and the ability to make collateral use of every spectrum to be collected on the SKA could provide further improvement to their limits will require further study.

In summary, we have demonstrated a sensitive and selective model-independent analysis technique for dark matter constituting our Galactic halo, based on only the most general assumed characteristics of its phase space structure. Signals that are both weak and broad ($\approx mJy$, $\frac{\Delta\nu}{\nu} \approx 10^{-3}$) can be readily detected at high confidence level. We wish to emphasize the generality of the method; while a very basic halo model has been used in this demonstration that is spherically symmetric and static, templates may be constructed for a halo of any arbitrary phase space and exclusion limits may be produced for it. In general, the individual contributions in the sum constituting the template will not be separable into a line integral and Doppler shift at each (l, b), but the procedure is trivially generalized. It should be noted that, while the technique here may not find any signature of dark matter, it may prove to be of utility in revealing weak conventional sources associated with the Galactic disk.

We gratefully acknowledge the support of the Heising–Simons Foundation, grant 2018-0989, and the assistance of Andrew Siemion, Steve Croft, and Matt Lebofsky of the Breakthrough Listen program throughout the project. The Breakthrough Prize Foundation funds the Breakthrough Initiatives, which manages Breakthrough Listen. The Green Bank Observatory facility is supported by the National Science Foundation and is operated by Associated Universities, Inc. under a cooperative agreement. We further thank Ben Safdi, Josh Foster, and Hitoshi Murayama for helpful discussions. A.K. acknowledges receipt of a graduate research grant from the Applied Science and Technology program, and N.R. acknowledges receipt of a Haas Scholars Fellowship. A.L. gratefully acknowledges a NSF California Alliance Postdoctoral Fellowship.

ORCID iDs

Aya Keller https://orcid.org/0000-0002-9036-3598

References

Akerib, D. S., Alsum, S., LUX Collaboration, et al. 2014, PhRvL, 118, 021303
Anastassopoulos, V., Aune, S., Barth, K., et al. 2017, NatPh, 13, 584
Aprile, E., Aalbers, J., XENON1T Collaboration, et al. 2019, PhRvL, 122, 141301
Ayala, A., Domínguez, I., Giannotti, M., Mirizzi, A., & Straniero, O. 2014, PhRvL, 113, 191302
Backes, K. M., Palken, D. A., HAYSTAC Collaboration, et al. 2021, Natur, 590, 238
Ballou, R., Deferne, G., Finger, M., et al. 2015, PhRvD, 92, 092002
Battaglieri, M., Belloni, A., Chou, A., et al. 2017, arXiv:1707.04591
Ben Bekhti, N., Flöer, L., Keller, R., et al. 2016, A&A, 594, A116
Blout, B. D., Daw, E. J., Decowski, M. P., et al. 2001, ApJ, 546, 825
Braine, T., Cervantes, R., ADMX Collaboration, et al. 2020, PhRvL, 124, 101303
Caputo, A., Regis, M., Taoso, M., & Witte, S. J. 2019, JCAP, 2019, 027
Cui, X., Abdukerim, A., PandaX-II Collaboration, et al. 2017, PhRvL, 119, 181302
Foster, J. W., Kahn, Y., MacIas, O., et al. 2020, PhRvL, 125, 171301
Isaacson, H., Siemion, A. P. V., Marcy, G. W., et al. 2017, PASP, 129, 054501
Kaneta, K., Lee, H.-S., & Yun, S. 2017, PhRvL, 118, 101802
Kuhn, H. W. 1955, Nav. Res., 2, 83
Lebofsky, M., Croft, S., Siemion, A. P., et al. 2019, PASP, 131, 1
Lee, S., Ahn, S., Choi, J., Ko, B. R., & Semertzidis, Y. K. 2020, PhRvL, 124, 101802
Monari, G., Famaey, B., Carrillo, I., et al. 2018, A&A, 616, L9
Murphy, D. 2019, RFI Scans and Known Sources, https://science.nrao.edu/facilities/gbt/interference-protection/ipg/rfi-scans
Navarro, J. F., Frenk, C. S., & White, S. D. M. 1997, ApJ, 490, 493
Nesti, F., & Salucci, P. 2013, JCAP, 2013, 016
Perryman, M. A. C., Lindegren, L., Kovalevsky, J., et al. 1997, A&A, 500, 501
Pillepich, A., Kuhlen, M., Guedes, J., & Madau, P. 2014, ApJ, 784, 161
Price, D. C., Enriquez, J. E., Brzycki, B., et al. 2020, AJ, 159, 86
Speckhard, E. G., Ng, K. C. Y., Beacom, J. F., & Laha, R. 2016, PhRvL, 116, 031301